


Modeling the Microstructure Evolution During Additive Manufacturing of Ti6Al4V: A Comparison Between Electron Beam Melting and Selective Laser Melting

G. VASTOLA ¹, G. ZHANG,^{1,2} Q.X. PEI,^{1,3} and Y.-W. ZHANG¹

1.—A*STAR Institute of High Performance Computing, 1 Fusionopolis Way #16-16, Connexis, Singapore 138632, Singapore. 2.—e-mail: zhangg@ihpc.a-star.edu.sg. 3.—e-mail: peiqx@ihpc.a-star.edu.sg

Beam-based additive manufacturing (AM) is an innovative technique in which parts are built layerwise, starting from the material in powder form. As a developing manufacturing technique, achievement of excellent mechanical properties in the final part is of paramount importance for the mainstream adoption of this technique in industrial manufacturing lines. At the same time, AM offers an unprecedented opportunity to precisely control the manufacturing conditions locally within the part during build, enabling local influence on the formation of the texture and microstructure. In order to achieve the control of microstructure by tailoring the AM machine parameters, a full understanding and modeling of the heat transfer and microstructure evolution processes is needed. Here, we show the implementation of the non-equilibrium equations for phase formation and dissolution in an AM modeling framework. The model is developed for the Ti6Al4V alloy and allows us to show microstructure evolution as given by the AM process. The developed capability is applied to the cases of electron beam melting and selective laser melting AM techniques to explain the significantly different microstructures observed in the two processes.

INTRODUCTION

Rapid prototyping differs from additive manufacturing (AM) in that the former is concerned with geometrical accuracy, while the latter adds a stringent requirement for the part's mechanical properties.¹ This requirement arises from the fact that AM parts not only need to be built but also to be put into service with an expected performance similar to, if not better than, corresponding cast parts (if available).² In AM, several factors contribute to the ultimate mechanical properties of the part, including the manufacturing technique,³ the presence of porosity, including incomplete melting,⁴ proper thermal control to avoid balling/overmelting,⁵ and the quality of the powder feedstock.⁶ Moreover, even at optimal build conditions, in which the former issues are minimized, a large role is played by the actual metal microstructure, which represents the ultimate factor that dictates the mechanical properties of the part.

Ti6Al4V is a pseudo-binary alloy with rich equilibrium⁷ and non-equilibrium⁸ phase diagrams. The main phases are represented by β , which is stable above 1000°C (beta transus),⁷ α , which is a diffusion-controlled phase stable below the beta transus, and martensite α' , which is α -competing and originates from diffusionless transformation of β under specific circumstances. From a traditional metallurgy point of view, Ti6Al4V has been extensively studied and significant works on it have been published.^{9–11} For example, Lütjering et al. have shown that the thickness of the α lath is the primary factor influencing strength and ductility.¹² In turn, the α lath thickness is controlled by the cooling rate after solidification, where faster cooling rates correspond to thinner α laths.¹³ Moreover, rapid quenching below the so-called martensite start temperature (T_{ms}) originates the α' phase, which is hard but brittle.¹⁴ Overall, metallurgy of Ti6Al4V has been very successful in showing the relationship between the microstructure and its mechanical properties.

Introduction of Ti6Al4V in AM opens tremendous opportunities for manufacturing complex shapes with industrial relevance, for example, cellular structures for lightweight aircraft components.¹⁵ Therefore, understanding how the AM process influences the part microstructure is of paramount importance. In this regard, the focus of this work will be on electron beam melting (EBM) and selective laser melting (SLM), which are among the main AM processes for Ti6Al4V. The primary footprint of these two techniques is that SLM produces samples with close to 100% martensite, while EBM (both powder bed and wire feed) produces milder alloys with fine α laths and retained β .³ At the same time, a more sophisticated control of microstructure would be highly desirable. For example, such control could allow the production of parts with locally tailored mechanical properties. In order to control the microstructure during AM builds, it is first necessary to understand how microstructure evolves during the AM process. In this regard, modeling is useful because it allows the study of the process under well-defined and constant process parameters, which is not necessarily the case in actual machine builds in which process parameters continuously change.

In this paper, we show the implementation of the non-equilibrium equations of microstructure evolution for Ti6Al4V in the framework of the additive manufacturing process simulation, where particular attention is paid to the modeling of martensite formation and decomposition. Using the finite element method (FEM) and starting from the solution of the thermal problem, we use the thermal field as input for the local microstructure calculation in terms of the volume fraction of each Ti6Al4V phase. The modeling allows us to show the evolution of the phases as the laser or electron beam travels across the domain. We apply the capability to both scenarios of SLM and EBM additive manufacturing. Our integrated thermal and microstructure model can be a useful tool for modelers and designers to understand and control microstructure evolution during additive manufacturing of Ti6Al4V.

MODEL

Modeling was based on the finite element method (FEM) in which the commercial software ABAQUS was used for meshing, solution, and post-processing. Customization for additive manufacturing, as well as for microstructure evolution, was implemented through user subroutines. Additive manufacturing was modeled by considering a two-dimensional (2D) mesh of length \times height of 5×1.2 mm. While such a size is small compared to common AM parts, our intention was to focus on a small mesh with fast convergence, which could show us the details of the thermal field as well as the microstructure evolution, which would be hindered at a larger scale. Addition of four layers of powder was considered, namely, the

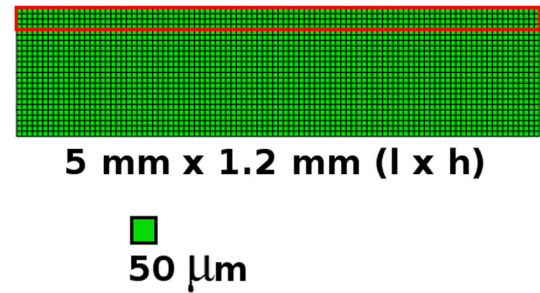


Fig. 1. Mesh employed in the simulations, which is composed of equal quadrilateral elements (4 integration points per element) with element size of $50 \mu\text{m}$. The red highlight shows the elements that are added during the simulation. Each layer of elements corresponds to one layer of powder (Color figure online).

simulation consisted in the sequential addition of elements, using the “element birth” technique. Between two subsequent layers, a representative inter-layer time of 0.5 s was used to model the time needed by the recoater to spread the new powder layer. The simulation domain is shown in Fig. 1. Element size was $50 \mu\text{m}$, which was one powder layer since the typical layer thickness for Ti6Al4V powder is $50 \mu\text{m}$.¹⁶ Quadrilateral, linear elements with four integration points were employed.

The first step of the simulation consisted in the solution of the thermal problem. Here, the beam was modeled as a traveling body heat source, with intensity in the SLM and EBM cases given by, respectively

$$I(x, z) = \frac{2AP}{\pi\omega^2} e^{\left(\frac{-2(x-vt)^2}{\omega^2}\right)} e^{-\frac{z}{d_0}} \quad (1)$$

$$I(x, z) = \frac{2AiV}{\pi\omega^2} e^{\left(\frac{-2(x-vt)^2}{\omega^2}\right)} \frac{1}{5} \left[-3\left(\frac{z}{d_0}\right)^2 - 2\frac{z}{d_0} + 5 \right] \quad (2)$$

where P is the laser power, A is the absorptivity ($A = 0.4$), i is the beam current ($i = 10$ mA), and V is the electron gun voltage ($V = 60$ kV). Consistent with experimental measures, the penetration depth was set to $40 \mu\text{m}$ for SLM¹⁷ and $28 \mu\text{m}$ for EBM.¹⁸ Scan speed was set to $v = 4.5$ m/s and beam size was $\omega = 250 \mu\text{m}$. Moreover, powder–liquid–solid phase transformations were implemented such that the material was explicitly described by a different set of material properties depending on the local phase. In particular, material properties were taken as in Ref. 19. A phase-change rule was implemented to allow phase change depending on local temperature. For example, if the local phase was “powder” and the temperature was rising above the liquidus, the local phase was changed to “liquid” and the corresponding material properties were used. Liquidus and solidus temperatures were taken as 1650°C and 1605°C , respectively, and latent heat was $286,000$ J/Kg.⁷ More details on the thermal modeling, including the implementation of the powder–liquid–solid phase changes, can be found in Ref. 20.

As the thermal problem was solved, the temperature evolution became available at each integration point of the mesh. In turn, temperature was used as input to a set of equations to describe the concurrent microstructure evolution. In particular, our modeling started from the work by Kelly and Babu²¹ to describe evolution of the α and β phases, where consideration for martensite α' formation and decomposition was added. At each integration point ζ , the volume fraction of α at thermodynamic equilibrium, $f_{\alpha,\text{eq}}$ was first computed. Following Charles-Murgau et al.,²² this quantity was calculated as

$$\begin{aligned} f_{\alpha,\text{eq}}(T) = & a_8(T/1000)^8 + a_7(T/1000)^7 + a_6(T/1000)^6 \\ & + a_5(T/1000)^5 + a_4(T/1000)^4 \\ & + a_3(T/1000)^3 + a_2(T/1000)^2 \\ & + a_1(T/1000) + a_0 \end{aligned} \quad (3)$$

where T is the temperature in $^{\circ}\text{C}$ and the numerical constants read $a_8 = -31188.514$, $a_7 = 170526.26$, $a_6 = -388991.69$, $a_5 = 471927.45$, $a_4 = -315178.49$, $a_3 = 99079.891$, $a_2 = 1667.1991$, $a_1 = -9726.8403$, and $a_0 = 1884.7280$. Moreover, the lower bound for β was ensured by imposing $\alpha_{\text{eq}} = 0.917$ for $T < 650^{\circ}\text{C}$. Then, the actual volume fraction of α was compared to α_{eq} and two scenarios arise, namely, $\beta \rightarrow \alpha$ if $f_{\alpha} < f_{\alpha,\text{eq}}$ and $\alpha \rightarrow \beta$ if $f_{\alpha} > f_{\alpha,\text{eq}}$. Both formation and dissolution of α were governed by Johnson–Mehl–Avrami equations of the form

$$F_{\alpha}(t, T) = (1 - e^{-kt^n})f_{\alpha,\text{eq}}(T) \quad (4)$$

where t is time, k is the kinetic rate of the phase transformation, and n is the Avrami coefficient. Both k and n are dependent on temperature, and details of their exact formulation have been reported in Ref. 21. The exact implementation of the equations, as well as the explicit value for the numerical coefficients, are reported in the Supplementary Material.

The diffusionless transformation $\beta \rightarrow \alpha'$ was modeled as a competitive mechanism to the formation of α . In particular, the following criteria was implemented: if the local temperature was below 800°C (martensite start temperature T_{ms} ¹⁶) and the local cooling rate was faster than 410°C/s ,²³ the available amount of β would transform into α' . Finally, decomposition of martensite was implemented from Gil Mur et al.,²⁴ namely, the volume fraction of recovered martensite upon heating was given by

$$\chi_r(t) = 1 - e^{-\beta t^k} \quad (5)$$

where both β and k were temperature-dependent and their numerical values were set as in Ref. 24. Upon decomposition, the assumption was made that α' was forming equilibrium α and β . In other words, naming $\delta\alpha$ and $\delta\beta$ the volume fraction changes of the respective phases during martensite decomposition, the following relationships were implemented:

$$\begin{cases} \delta f_{\alpha} + \delta f_{\beta} = -\delta f_{\alpha'} \\ \frac{\delta f_{\alpha}}{\delta f_{\beta}} = \frac{f_{\alpha,\text{eq}}}{1-f_{\alpha,\text{eq}}} \end{cases} \quad (6)$$

where $f_{\alpha'}$ is the change in martensite volume fraction at time t . Machine specifications of EBM and SLM were modeled as follows. The sample free surface (i.e., the free surface of the topmost layer of elements, independently of the number of layers built) was allowed to exchange heat through convection and radiation in the case of SLM, while only through radiation for the case of EBM. The heat convection coefficient was taken from Ref. 25 and Ti6Al4V emissivity was set to 0.7.⁷ The difference in preheating strategy between SLM and EBM was considered by setting the initial domain temperature, as well as the fixed temperature of the boundary nodes to 700°C for the case of EBM, and to 30°C for the case of SLM.

RESULTS AND DISCUSSION

We begin by validating our microstructure implementation by directly comparing our computed phases volume fraction with that of Kelly.²¹ At this preliminary stage, the specifications of the AM build are not yet activated, and the FEM domain is used as a block of Ti6Al4V in which the temperature of the entire domain is prescribed to the path shown in Fig. 2a. Under these circumstances, the predicted volume fraction of α , and the comparison with the original implementation by Kelly, is shown in Fig. 2b. Further checks showed that the slight discrepancy in the predicted f_{α} during the second cooling stage was to be ascribed purely to our choice of reference for α_{eq} (Eq. 3). Therefore, the level of agreement was considered satisfactory and modeling was continued by activating the beam heat source and heat boundary conditions specific to AM. Moreover, the domain was set with initial material of “powder” with enabled powder–liquid–solid phase changes. The initial condition for the microstructure was set to 91% α , corresponding to 9% of retained β , as measured by Malinov *et al.*²⁶

Representative snapshots of the temperature and of the microstructure evolution are shown in Figs. 3 and 4, respectively, where the blue and red colors represents the volume fraction of β and α phase, respectively. In particular, as the beam travels across the powder and melts it, the temperature increases above the beta transus, and in fact the local phase is 100% β . Later, as the material cools, β progressively transforms into α . At this point, a distinction between α and α' is not made yet, in the sense that the volume fraction of α' is incorporated into that of α . A focus on the martensite component will be the subject of the next paragraph. As α tries to reach its thermodynamic equilibrium, its volume fraction increases. This increase is shown in Fig. 4 by the progressive increase of α behind the melt

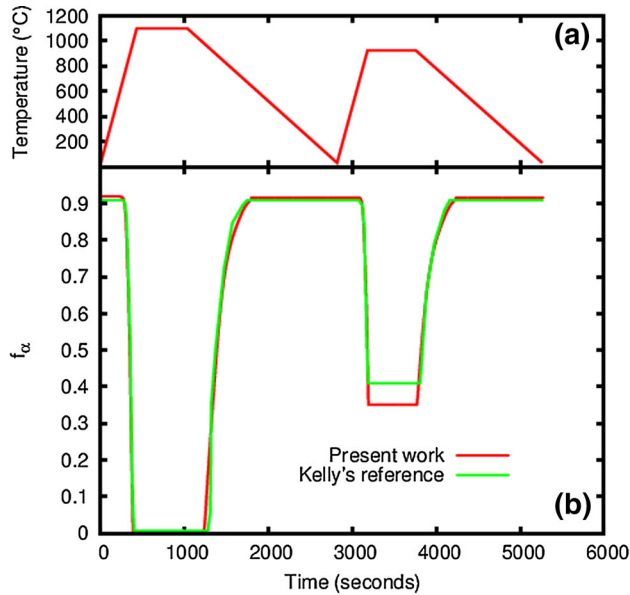


Fig. 2. Validation of the implemented equations for microstructure evolution compared to the reference work of Kelly.²¹ Using the mesh domain of Fig. 1 as a solid block without additive manufacturing features, the mesh was constrained to follow the temperature path shown in (a). During temperature evolution, volume fraction of α phase was recorded and compared to the one computed in Ref. 21 (b). (a) and the green curve in (b) are adapted with permission from Ref. 21.

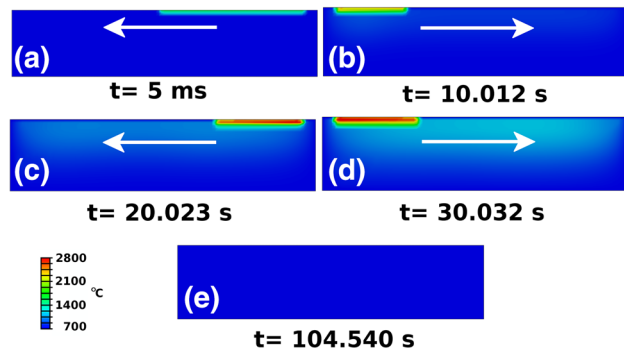


Fig. 3. Evolution of the temperature field during addition of four layers of powder. The arrow shows the direction of movement of the beam on each layer. Notice the heat accumulation at the sides of the scan track, caused by the low thermal conductivity of the powder compared to that of the bulk metal.

pool, and also during the interlayer cooling time before deposition of two subsequent layers. Moreover, it is shown that the scan of the following layer has indeed a clear effect on the microstructure of the layers below. In particular, heat is sufficient to transform α into β through a thickness of about ~ 10 equivalent powder layers. This result shows that, indeed, materials processing in additive manufacturing is characterized by multiple cycles of heating and cooling above and below the beta transus.

Next, our focus was on the formation and dissolution of martensite. To this end, two simulations were designed to represent the typical conditions of

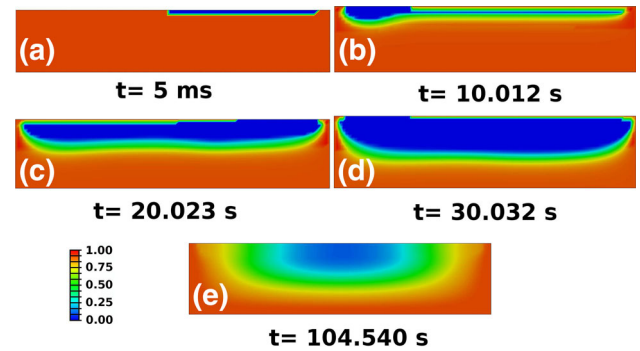


Fig. 4. Evolution of the volume fraction of α phase at the same time frames as in Fig. 3. As the local temperature exceeds the beta transus, the alloy is purely in β phase (blue color). Later, as the material cools, α nucleates from β with time dependence dictated by Eq. 4 in the text. Notice that, after deposition and scanning of a subsequent layer, the heat distribution is sufficient to transform α into β at a considerable depth from the free surface, of around ten equivalent build layers. Finally, after the last layer is scanned, cooling induces the final transformation of β into α , which also involves the entire domain and not only the upper layer of material (Color figure online).

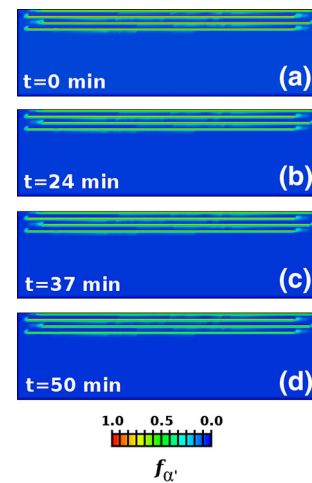


Fig. 5. Evolution of the volume fraction of martensite α' after completion of the four-layer scan, for a simulation in which machine parameters from selective laser melting were taken, in particular, where the boundary temperature was kept fixed at 30°C . (a) Martensite distribution immediately after scan of the fourth layer. (b)–(d) Limited martensite decomposition even after 50 min from the end of the build, because the domain temperature is not high enough to allow a significant rate of decomposition.

an EBM and a SLM machine, respectively. Here, because of the importance of resolving as many microstructure details as possible, a choice was made to halve the mesh size to $25\ \mu\text{m} \times 25\ \mu\text{m}$. Specifically, the two simulations differ in the heat source profile, the heat exchange at the free surface, and the preheating temperature, as described in the “Model” section. Under these conditions, the volume fraction of martensite at the end of the scanning of the four layers is shown in Figs. 5 and 6 for SLM and EBM, respectively. Comparison between the two panels shows the formation of martensite in both cases, with slight variations in terms of qualitative

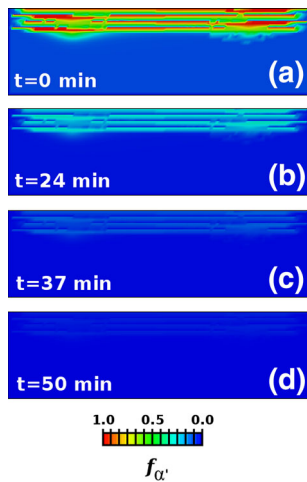


Fig. 6. Same evolution as in Fig. 5, except for the machine parameters which are now set for electron beam melting, in particular, where the boundary temperature was kept fixed at 700°C. (a) Martensite distribution immediately after scan of the fourth layer. (b)–(d) Complete martensite decomposition due to the relatively high domain temperature, allowing high kinetic rate for martensite decomposition.

distribution. In particular, the distribution α' is shown to be more abrupt in the case of SLM than in EBM. This feature can be understood by recalling the lower build temperature, and therefore the sharper thermal gradients, that characterize SLM and therefore that limit the region of the sample where the conditions for martensite formation are met.

After scanning was complete, the material was allowed to anneal by keeping the boundary temperature constant. Figures 5 and 6 show the evolution of as-built martensite and, in particular, suggest that martensite decomposition is complete in EBM, while martensite is still mostly retained in SLM. This result is in agreement with actual manufacturing, where SLM samples consistently have more martensite than EBM samples.³ Indeed, further evidence of martensite formation and subsequent decomposition was recently found for EBM processing.¹⁶

CONCLUSION

In summary, we developed a numerical scheme in which the heat transfer and microstructure evolution equations are coupled for the additive manufacturing of Ti6Al4V parts. The simulations have shown that the heat transfer arising from material processing is sufficient to induce microstructure evolution through several layers below the free surface, and in particular to a depth of up to 10 layers. This result suggests that proper microstructure control has to be achieved by taking into account the effect of not only the first scan but also of the next few in determining the final microstructure. Formation and dissolution of martensite was studied in the context of comparing EBM to SLM

processing. Given the two different processing temperature conditions, it was shown that EBM manufacturing allows for complete decomposition of martensite after build, while SLM mostly retains the martensite. Globally, our modeling represents a specific tool to understand and predict microstructure evolution in powder-bed additive manufacturing, and can help to find the choice of process parameters to locally control the microstructure which, in turn, allows the control of the final mechanical properties of the part.

ACKNOWLEDGEMENTS

The authors acknowledge helpful discussions with Dr. W. Pan and S.M.L. Nai at A*STAR Singapore Institute of Manufacturing Technology (SIMTech), and X. Tan and Prof. S.B. Tor at Nanyang Technological University. This work was supported by the Agency for Science, Technology and Research of Singapore through the Industrial Additive Manufacturing Program (Grants 132 550 4103 and 132 550 4106).

REFERENCES

1. D. Bourell, D.W. Rosen, M. Leu, *3D Print. Addit. Manuf.* 1(1), 6 (2014).
2. T. Wohlers, ed., *Wohlers Report 2015* (Wohlers Associates, Fort Collins, Colorado, 2015).
3. H. Rafi, N. Karthik, H. Gong, T. Starr, B. Stucker, *JME-PEG* 22, 3872 (2013).
4. H. Gong, K. Rafi, T. Starr, B. Stucker, *Proceedings of the Solid Freeform Fabrication Symposium* (2013), pp. 424–439.
5. M. Zäh, S. Lutzmann, *Prod. Eng. Res. Devel.* 4, 15 (2010).
6. H. Tang, M. Qian, N. Liu, X. Zhang, G. Yang, J. Wang, *JOM* 67, 555 (2015).
7. G. Welsch, R. Boyer, and E. Collings, *Materials Properties Handbook: Titanium Alloys*, Chap. Alpha-Beta Alloys (ASM International, Russell, OH, 2007), p. 516.
8. J. Sieniawski and W. Ziaja, eds., *Titanium Alloys - Advances in Properties Control* (InTech, 2013).
9. S. Semiatin, T. Bieler, *Acta Mater.* 49(17), 3565 (2001).
10. S. Semiatin, S. Knisley, P. Fagin, D. Barker, F. Zhang, *Metal. Mater. Trans. A* 34(10), 2377 (2003).
11. S. Zherebtsov, M. Murzinova, G. Salishchev, S. Semiatin, *Acta Mater.* 59(10), 4138 (2011).
12. G. Lütjering, *Mater. Sci. Eng. A* 243(1–2), 32 (1998).
13. F. Gil, J. Manero, M. Ginebra, J. Planell, *Mater. Sci. Eng. A* 349(1–2), 150 (2003).
14. K. Kubiak, J. Sieniawski, *J. Mater. Process. Technol.* 78(1–3), 117 (1998).
15. S. Campanelli, N. Contuzzi, A. Ludovico, F. Caiazzo, F. Cardaropoli, V. Sergi, *Materials* 7, 4803 (2014).
16. X. Tan, Y. Kok, Y.J. Tan, G. Vastola, Q. Pei, G. Zhang, Y.-W. Zhang, S. Tor, K. Leong, C. Chua, *J. Alloys Comp.* 646, 303 (2015).
17. R. McVey, R. Melnychuk, J. Todd, R. Martukanitz, *J. Laser Appl.* 19, 214 (2007).
18. M. Jamshidinia, F. Kong, R. Kovacevic, *J. Manuf. Sci. Eng.* 135, 061010 (2013).
19. A.N. Arce, *Thermal Modeling and Simulation of Electron Beam Melting for Rapid Prototyping on Ti6Al4V Alloys* (PhD thesis, North Carolina State University, 2012).
20. G. Vastola, G. Zhang, Q. Pei, Y.-W. Zhang, *Addit. Manuf.* 7, 57 (2015).
21. S. M. Kelly, *Thermal and Microstructure Modeling of Metal Deposition Processes with Application to Ti-6Al-4V* (PhD thesis, Virginia Polytechnic Institute and State University, 2004).

22. C. Charles-Murgau, *Modelling Microstructure Evolution of Weld Deposited Ti-6Al-4V* (PhD thesis, Luleå University of Technology, 2008).
23. T. Ahmed, H. Rack, *Mater. Sci. Eng. A* 243(1–2), 206 (1998).
24. F.G. Mur, D. Rodríguez, J. Planell, *J. Alloys Compd.* 234(2), 287 (1996).
25. I. Yadroitsev, I. Smurov, *Phys. Proc.* 12A, 264 (2011).
26. S. Malinov, Z. Guo, W. Sha, A. Wilson, *Metal. Mater. Trans. A* 32(4), 879 (2001).